13th International Symposium on Turbulence and Shear Flow Phenomena (TSFP13)
Montreal, Canada, June 25–28, 2024

THE EFFECT OF FREESTREAM TURBULENCE ON WING TIP VORTEX MEANDERING

Marie Couliou
DAAA
ONERA
Institut Polytechnique de Paris
8 rue des Vertugadins, Meudon, 92190, France
marie.couliou@onera.fr

Girish K. Jankee, Srikar Yadala Venkata, Ingrid Neunaber and R. Jason Hearst
Department of Energy and Process Engineering
Norwegian University of Science and Technology
Kolbjørn Hejes vei 2, 7034 Trondheim, Norway

ABSTRACT

The effect of freestream turbulence (FST) on a wing tip vortex was investigated at a chord-based Reynolds number of $Re_c = U_\infty c/\nu = 1.04 \times 10^5$. Experiments were conducted at four FST levels, 0.30%, 1.84%, 7.70%, and 13.25 %, generated by an active grid. Stereoscopic PIV measurements document the effects of freestream turbulence on the meandering motion of the wing tip vortex at the near field and middle field of a NACA0012 wing, i.e., planes $x/c = [2,5]$ downstream from the trailing edge of the wing. Conditional averaging based on recentring the coordinate system on the vortex center has been used to eliminate the influence of vortex motion. When the analysis was conditionally averaged on the vortex's core position, a reduction in vortex strength with increasing FST, along with a slight increase in diffusion was observed for the highest FST. Snapshot proper orthogonal decomposition analysis on the coherent component of the streamwise vorticity field revealed two dominant modes associated with meandering displacement for all FST. For the highest turbulent case, vortex deformation instability modes, not present at low FST, appear.

INTRODUCTION

Wing tip vortices are of particular interest in aeronautical applications due to their significant contribution to the overall drag of an aircraft and their persistence in flight corridors and runways, posing potential hazards and flight safety concerns (Gerz *et al.*, 2002). Numerous studies such as Spalart (1998), have focused on the evolution of wing tip vortices, acknowledging their susceptibility to a multitude of factors including Reynolds number, angle of attack, ground proximity, atmospheric freestream turbulence, buoyancy, wind shear, etc. Several experimental studies (Sarpkaya & Daly, 1987; Devenport *et al.*, 1996) explored wing tip vortices, considering factors such as Reynolds number and freestream turbulence. A common feature of trailing vortices is the time-dependent deformation or motion of their axes, a phenomenon referred to as vortex meandering. It is commonly described as being long-wavelength and random (Devenport *et al.*, 1996; Heyes *et al.*, 2004). Incoming turbulence, often referred to as freestream turbulence (FST), exerts an influence on wing tip vortices and, consequently, vortex meandering (Ghimire & Bailey, 2017). Studies by Bailey *et al.* (2018) and Ben Miloud *et al.* (2020) have demonstrated FST's role in vortex decay, strength, and meandering in the near wake field.

The objective of the present study was to identify and document the effects of FST generated by an active grid (Makita, 1991), on the meandering motion of a wing tip vortex. While many previous researchers have addressed and, to some extent, elucidated various aspects of vortex meandering, there have been very few measurements conducted at high FST intensities in both the near and middle fields of the wing. This will be further investigated in this article.

EXPERIMENTAL SET-UP

Wind tunnel, wing and flow conditions

The experiments were conducted in the large-scale closed-loop wind tunnel at the Norwegian University of Science and Technology. The wind tunnel has a test-section with dimensions of 2.71 m $\times$ 1.8 m $\times$ 11 m (width $\times$ height $\times$ length). The roof of the tunnel is adjustable and gradually increases to create a near-zero-pressure-gradient along the length of the test-section. The wind tunnel is fit with an active turbulence grid which enables the generation of high intensity turbulent flows upstream of the wing. The particular active grid used in this facility is described in detail by Kildal *et al.* (2023). The active grid spans the entirety of the test section's cross-sectional area and consists of 90 shaft assemblies, with each assembly being individually operated by a dedicated integrated stepper motor. The mesh length of the grid is $M = 0.1$ m. Four test cases were generated for this study: REF, A, B, and C. The active grid was removed for REF case, producing a relatively clean incoming flow. For case A the active grid was in place but kept static and fully open, producing a turbulent flow with low intensity. For case B, only the vertical axes of the active grid were spinning randomly with rotational velocities distributed in the range 7 ± 2 Hz. For case C all active grid axes were spinning randomly within the range 2 ± 2 Hz pro-

ducing increasing levels of turbulence intensity based on the 'fully random' methodology of Hearst & Lavoie (2015).

The wing tip vortices are generated by an airfoil with a NACA0012 symmetric profile of chord length $c = 0.125$ m and wing span $b = 0.5$ m. The airfoil is mounted to a sting with a NACA0015 profile with a chord length of 0.045 m and a length of 0.506 m which is in turn mounted to an extruded aluminum profile attached to the wind-tunnel floor. The wing trailing edge is placed at 0.945 m from the floor (mid height of the wind tunnel at the location of measurement) and 6.7775 m downstream of the active grid. The angle of attack is set to $-9°$. Hereafter, the z-axis is inverted to be comparable to previous studies (Bölle *et al.*, 2023) and has a corresponding wing with an angle of attack of 9°. The experiments were conducted at a mean velocity of $U_\infty = 13$ m/s, corresponding to a chord-based Reynolds number $Re_c = U_\infty c/\nu = 1.04 \times 10^5$ where U_∞ is the freestream velocity, c is the wing chord length, and ν is the air kinematic viscosity. The x, y, and z axes were aligned with the streamwise, transverse, and vertical directions of the wind tunnel reference frame, respectively. The origin of the coordinate system (X_0, Y_0, Z_0) is located at the left trailing tip of the airfoil with X_0 at 6.7775 m $= 54.22c = 66.525M$, downstream of the active grid, Y_0 at 0.25 m from the middle of wind tunnel and Z_0 at 0.945 m from the floor.

Metrologies

To measure the turbulence statistics of the incoming flows without the wing present, a hot-wire probe was fixed close to a Pitot-static tube and a temperature probe on the four-degree-of-freedom wind tunnel traverse. A Dantec 55P11 single hot-wire probe, controlled by a Dantec StreamLine Pro constant temperature anemometer, was employed. The hot-wire was sampled at a nominal acquisition rate of 75 kHz, with an analog low-pass cutoff filter set to 30 kHz. Hot-wire samples were acquired for 600 seconds.

Cross-stream stereoscopic PIV (SPIV) measurements were performed in the y-z plane at 2 different streamwise locations, namely x/c of 2 and 5. A Photonics *DM 100-532 DH* 10 mJ dual pulse Nd:YAG high speed laser was used to create a laser sheet with a thickness of roughly 1 mm. Two Phantom *V2012* 1 MP high speed cameras were locked at a mean angle of 40° with respect to the region of interest. For each test case, 12442 image pairs at 0.101 kHz were captured. Image acquisition, pre-processing, and vector field computation were performed using the LaVision Davis 10 software suite. Cross-correlation of the vector field was carried out using multiple passes starting from 96×96 px^2 down to 48×48 px^2 circular-shaped windows as the final pass with an overlap of 50%. This resulted in a spatial resolution of 4.5 mm per vector in both the y- and z-directions.

RESULTS

Flow conditions

A preliminary study of flow homogeneity in the empty wind tunnel was performed with hot-wire anemometry to understand the incoming flow conditions produced for the various test cases. At the location of the wing trailing edge i.e., 6.77 m $= 54.22c = 66.525M$ downstream of the active grid, the four cases produced turbulence intensities T_i of 0.30, 1.84, 7.70, and 13.23% for cases REF, A, B, and C, respectively, as a result of the natural streamwise decay of grid-generated turbulence. In the present configuration, the integral scale and intensity increased together, representing larger scale and more intense turbulence. L_{11}/M the integral scale non-dimensionalised by mesh length M is 0.06, 0.22, 0.32 for cases A, B, and C, respectively, based on the hot-wire measurements (Table 1).At 5 chords downstream of the wing, turbulence intensities slowly decrease to 0.26, 1.71, 7.34, and 12.35% for cases REF, A, B, and C, respectively.

Table 1. Turbulence properties in the empty wind tunnel at the wing trailing edge location ($x/c = 0$)

Case	Grid Mode	U_∞ [m/s]	T_i [%]	L_{11}/M	Re_λ
REF	(no grid)	12.96	0.30	-	-
A	(static)	12.93	1.84	0.06	62
B	(vertical)	13.00	7.70	0.22	370
C	(all)	12.58	13.23	0.32	580

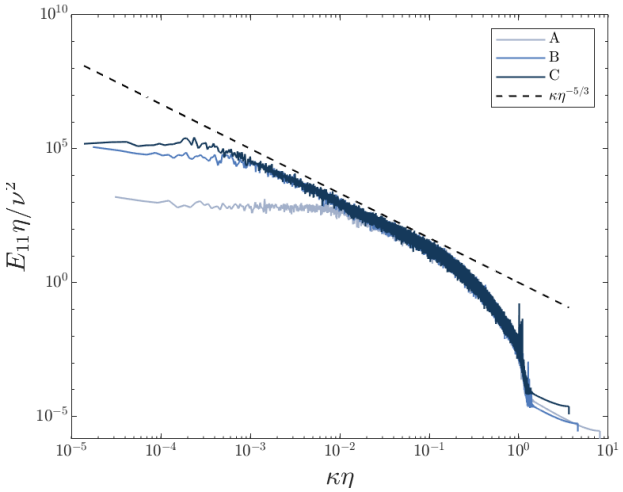

Figure 1. Velocity spectra for turbulent cases (A,B,C) at $x/c = 0$ plotted in wavenumber-space normalised by dissipative scales.

Table 1 summarizes the main turbulent flow conditions of the empty wind tunnel measured at the wing trailing edge location i.e. $x/c = 0$. The table includes values for the mean freestream velocity, the turbulence intensity, the integral length scale, and the Taylor microscale-based Reynolds number Re_λ. The turbulent velocity spectra obtained from the hot-wire measurements for all cases are shown in Figure 1.

The frequency and power axis were plotted on a logarithmic scale and non-dimensionalized with η, as the Kolmogorov length, κ, as the wavenumber, and ν, as the kinematic viscosity. Viscous unit normalisation is used and all turbulent spectra collapse at the small scales and differ at the large scales, as one might expect. A $(\kappa\eta)^{-5/3}$ line is added for reference. The absence of low-frequency peaks in the spectra indicates that the active grid forcing does not preferentially energize a particular frequency or set of frequencies, which is the desired outcome. As the turbulence intensity increases, the inertial range grows, as expected from previous active grid measurements (Larssen & Devenport, 2011) and theory for increasing Re_λ. However, some differences in the inertial sub-range and the energy distribution for the lowest frequencies between the three cases should be noted. In particular, and in agreement with Larssen & Devenport (2011), the random ATG cases had a larger in-

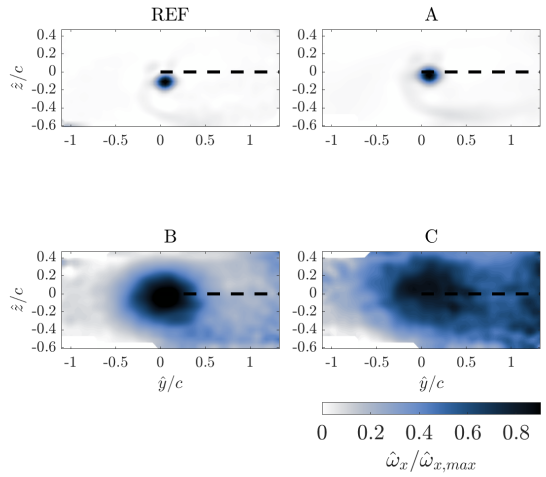

Figure 2. Contours of the normalized averaged axial vorticity $\hat{\omega}_x/\hat{\omega}_{x,max}$ at $x/c = 5$.

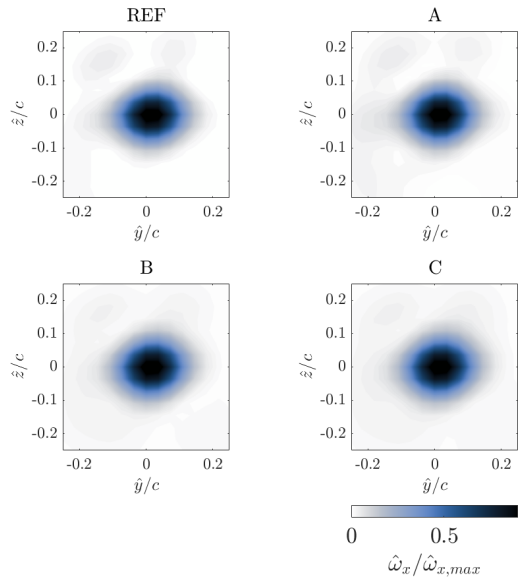

Figure 3. Contours of the normalized conditional averaged streamwise vorticity $\hat{\omega}_x/\hat{\omega}_{x,max}$ at $x/c = 5$.

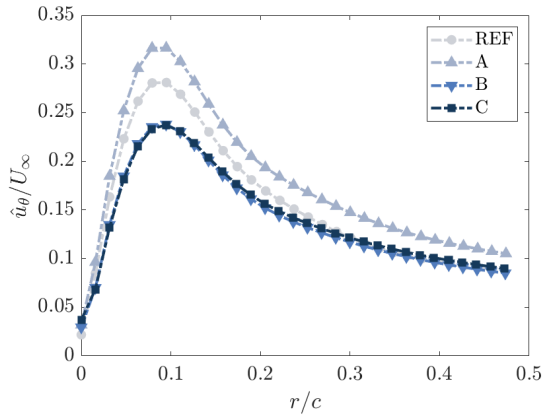

Figure 4. Normalised azimuthal core conditional averaged velocity profiles for each turbulent case at $x/c = 5$

ertial sub-range, suggesting a greater range of scales in the flow. Additionally, the energy contained in the flow for low frequencies is greater in the most turbulent cases, indicating an increase in kinetic energy in the flow.

Effect of FST on wing tip vortex statistics

This section focuses on the analysis of statistical properties extracted from the SPIV data. This analysis was performed on the wing tip vortex properties at a given streamwise plane at $x/c = 5$.

The contour maps of the time-averaged streamwise vorticity $\omega_x = \frac{\partial w}{\partial y} - \frac{\partial v}{\partial z}$ at $x/c = 5$ for the tested cases are presented in Figure 2. To ensure a consistent colour scale across all cases, the maximum vorticity at the vortex center $\hat{\omega}_{x,max}$ was used for vorticity normalization.

In Figure 2, the vortex was identified by a high concentration of vorticity near the wing tip. It is noteworthy that the maximum values of dimensional vorticity decreased with increasing FST. The vorticity contours for the different test cases appeared to grow with increasing FST. The wake shear layer around the vortex concentration area is well-defined in all cases which is consistent with the fact that the vortical shear layer is still rolling up into well-defined concentrated vortices at the measurement plane five chord lengths downstream of the wing. Moreover, as FST intensity increased, particularly in cases B and C, vorticity contours appeared more diffused compared to the reference case without a grid (REF), covering a larger area around the vortex core.

To investigate the alterations in vortex meandering induced by FST, all the fields were then analyzed using conditional averaging based on recentring the coordinate system on the vortex center. The velocity fields, and thus the vorticity fields, have been averaged across the frames after adjusting each instantaneous field to be recentered with the vortex at the origin, i.e., $(\hat{y}, \hat{z}) = (0,0)$. The initial step in the post-processing of the PIV field is the identification of the vortex center. This detection process is carried out in two phases. Initially, we determine the instantaneous extremum position (y_m, z_m) with m representing the location of the maximum axial vorticity ω_x. By construction, (y_m, z_m) is restrained to the vertices of the PIV mesh. To refine this localization, we then calculate $\mathbf{x}_\omega$ the barycenter of the axial vorticity over a reduced region Ω_m centered about $\mathbf{x}_m$. The integration area Ω_m is taken as a disk of radius $0.12c$ for all the tests. This region was found to be large enough to contain the core of the vortex, while excluding the freestream turbulence. The resulting contours of the normalized conditional averaged streamwise vorticity $\hat{\omega}_x/\hat{\omega}_{x,max}$ are plotted in Figure 3. We observe that the averaged vortex size, as determined by the vortex core radius, remained fairly constant as FST increased. The shape of the vortex does not have a strong dependence on the FST. From these conditional averaged axial vorticity fields, the maximal streamwise vorticity $\hat{\omega}_{x,max} * c/U_\infty$ is extracted and is found to be [9.86;11.13;8.15;8.0] for cases [REF;A;B;C]. Interestingly, the maximal streamwise vorticity is not at the highest values in the clean flow case (Case REF) but in the low turbulence case (Case A). $\hat{\omega}_{x,max} * c/U_\infty$ then decreases as FST increases suggesting a diffusion of the vortex with increasing FST in agreement with Pentelow (2014) and Ben Miloud *et al.* (2020).

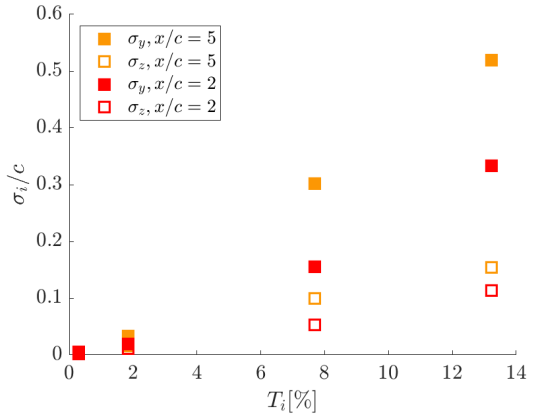

Figure 5. Variation of meandering amplitudes σ_i/c with incoming turbulence intensity T_i

The conditional average of the vortex azimuthal velocity was evaluated as a function of the radial distance r in Figure 4. The azimuthal velocity was determined by using the velocity components $\hat{v}$ and $\hat{w}$ in the Cartesian coordinate system, converting them into polar coordinates, as: $\hat{u}_\theta = \hat{w}cos(\theta) - \hat{v}sin(\theta)$.

Figure 4 shows the evolution of the azimuthal velocity profile as a function of r with $r = 0$ the center of vortex - defined as the barycenter of vorticity of the conditional averaged vorticity field- and for the different FST. Similar to the maximal vorticity, the peak azimuthal velocity is maximum for the low turbulence case (Case A) and then decreases as FST increases. The profile of the azimuthal velocity can be used to characterize the vortex size as the vortex core radius, i.e., the radius of maximum azimuthal velocity defined as r_c. One can see in Figure 4 that r_c remains constant around $0.95c$ for all cases. This averaged value is consistent with observations from the literature, e.g., Ben Miloud *et al.* (2020), but also in contrast to Ben Miloud *et al.* (2020) we do not observe a dependence of the vortex core radius for the strongest FST.

To determine the meandering amplitudes in the transverse and vertical directions, denoted σ_y and σ_z, respectively, the standard deviations of the time series for the vortex axis displacements from the mean position were calculated for each direction. The dependence of these amplitudes on the incoming turbulence intensity is presented in Figure 5. As the vortex was convected to $x/c = 5$, the meandering amplitudes are larger than those at $x/c = 2$ meaning the area covered by the scatter of the instantaneous vortex center positions is increasing particularly for the highest FST intensity. This is expected and noted by Bailey *et al.* (2018) (their highest T_i was 5%) and Ben Miloud *et al.* (2020) (their highest T_i was 6%) as well as the meandering amplitudes which strongly increased in both directions with FST. For highest T_i cases in the current study, which are above the 6% achieved in previous studies (Bailey *et al.*, 2018; Ben Miloud *et al.*, 2020), a preferential direction (y-direction) is observed; σ_y is 3 times larger than σ_z at both x-planes ($x/c = 2$ and $x/c = 5$).

Proper orthogonal decomposition analysis

To investigate the effect of the FST on the wing tip vortex dynamics, proper orthogonal decomposition (POD) is used. The *snapshot* formulation of POD proposed by Sirovich (1987) is employed for this purpose. A detailed description of *snapshot-POD* can be found in Sirovich (1987) or the review by Taira *et al.* (2017). Given that we want to capture the full vortex dynamics, the unconditioned vorticity field is used. Snapshot-POD was applied on the time-series of streamwise vorticity field. In particular, the fluctuating streamwise vorticity $\tilde{\omega}_x$ (with $\omega_x = \hat{\omega}_x + \tilde{\omega}_x$) was decomposed in the following manner:

$$\tilde{\omega}_x(\hat{y},\hat{z},t) = \sum_n \gamma_n \Theta_n(t) \Psi_n(\hat{y},\hat{z}), \tag{1}$$

where $\Psi^n(\hat{y},\hat{z})$ are a set of empirical eigenfunctions (spatial POD modes) that contain information regarding the spatial organisation of various fluctuations with corresponding eigenvalues γ_n representing the modal energy and temporal coefficients $\Theta(t)$, where n represents the mode number. The modes are sorted in descending order of their relative modal energy. We focus on the location $x/c = 5$ for the present analysis.

The spatial organisation of fluctuating fields $\tilde{\omega}_x$ at $x/c = 5$ is plotted in Figure 2. In the reference case (REF), modes 1 and 2 (Figure 6.(a) and Figure 6.(d)) exhibit 2 polar fluctuations at the tip. As explained by Fabre *et al.* (2006), this dipole aligns with the helical displacement pattern of the vortex and in the present case it is the signature of the meandering of the vortex as observed by Dghim *et al.* (2021). For mode 2, some fluctuations are also observed below the wing but are less intense than the ones at the tip location. For modes 3 to 15 (only modes 3 and 4 are shown in Figure 6.(g) and Figure 6.(j)), the fluctuations are located below the wing. They can be associated with the vorticity sheet, which has not yet rolled up into the vortex at $x/c = 5$.

For case A (low turbulence level), modes 1, 2, 3, and 4, shown in Figure 6.(b), Figure 6.(e), Figure 6.(h), and Figure 6.(k), are located at the tip of the wing and thus at the wing tip vortex. Indeed, in that case, as visible in Figure 2 at $x/c = 5$, the vortex is well defined around $(\hat{y},\hat{z}) = (0,0)$. Note that the modes located in the vorticity sheet do not appear before mode 7 and represent less than 1% of the total energy. For case A, modes 1 and 2 are plotted in Figure 6.(b) and Figure 6.(e). A similar spatial organization of the first two modes of the REF case is observed. Thus, we associate them also with vortex displacement modes. As described by Leweke & Le Dizès (2016), POD mode 3 and mode 4 of the present study exhibit spatial organisation typically of vortex deformation modes as the bending mode and double-helix mode of elliptic instability modes.

The first four POD modes are plotted for case B in Figure 6.(c), Figure 6.(f), Figure 6.(i), and Figure 6.(l). Case B mirrors Case A but over a larger spatial area. For the meandering modes (modes 1 and 2), this implies that displacements are expected to occur with larger motion. This is consistent with the larger meandering amplitude observed in Figure 5. For case C (not shown), characteristics remain consistent with cases A and B, but over an even larger spatial area, which limits mode observation due to the restricted field of view.

The relative energies of the first ten POD modes corresponding to cases REF, A, B, and C, are presented in Figure 7. For test cases REF, B, and C, the energy of the first three POD modes is much smaller compared to those in case A. In the REF case, the FST is very low, and the vortex is quite stable, thus the low modal energies compared to the others are coherent with the expected low fluctuations.

In case A, the energy of subsequent modes decreases monotonically, with the first mode containing $\approx 35\%$ of the total energy. Despite the spacial organisation similarity, note

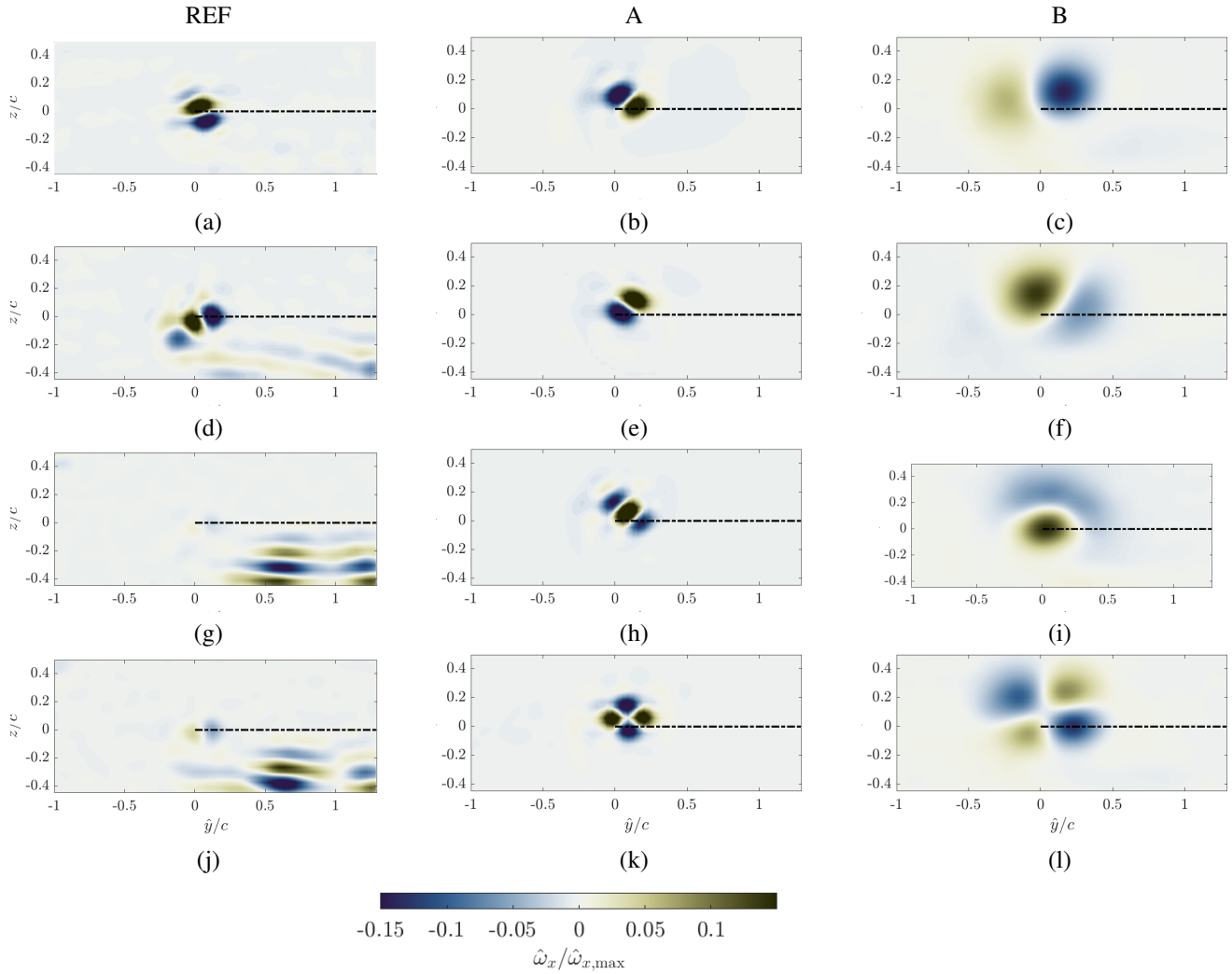

Figure 6. Spatial organisation of nondimensioned fluctuating fields $\tilde{\omega}_x$ at $x/c = 5$ corresponding to POD eigenmodes $n = 1$ (a-c), $n = 2$ (d-f), $n = 3$ (g-i), $n = 4$ (j-l) for cases REF (a, d,g,j), A (b, e,h,k) and B (c, f,i,l).

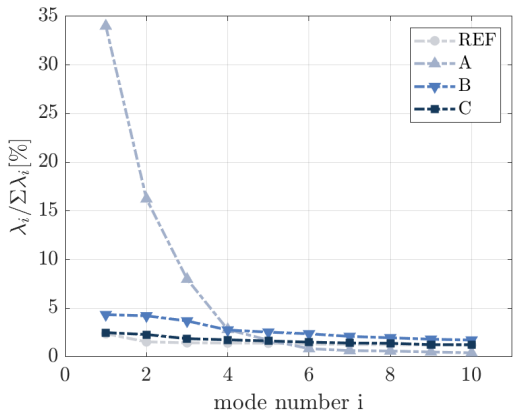

Figure 7. Relative energies of the first 10 POD eigenmodes for cases REF, A, B and C at x/c=5

that the energy of these modes is significantly more important for case A than for other cases (Figure 7). It is particularly true for the meandering modes which are the principal modes for all cases but represent 50% of the total energy for case A, instead of less than 10% for cases REF, B, and C. We hypothesize a physical reason: for the REF case all dynamics are weak while for "high" turbulence (cases B and C) other features (like deformations) appear due to the turbulence effects and redistribute modal energy. In contrast, for case A, the vortex only feels the meandering. To summarize, independently of the level of turbulence, the 2 first POD modes are associated with the meandering motion. For the lowest FST case REF, the other modes are linked to the dynamics of the vorticity sheet. For higher FST, deformation modes are triggered by the turbulence and appear. The higher the FST is, the larger the area of displacement and deformation regions of the vortex are.

CONCLUSIONS AND OUTLOOK

SPIV measurements combined with the use of an active grid enabled us to document the effects of freestream turbulence on the meandering motion of a wing tip vortex in the near field and middle field downstream of a wing.

First, the statistical analysis, conditioned on the vortex's core position, reveals a reduction in vortex strength with increasing FST, coupled with a modest augmentation in diffusion. The amplitude of vortex meandering amplifies proportionally with FST. The findings corroborate prior studies, e.g., Dghim *et al.* (2021). Notably, a novel finding with significant implications for understanding vortex behavior in the presence of high turbulence levels is that at highest FST levels

($T_i > 6\%$), a preferential orientation in the meandering motion towards one direction is observed. It remains unclear why a selective orientation occurs, suggesting the need for further investigation in future works.

The wing tip vortex exhibits the highest levels of maximum vorticity, azimuthal velocity, and meandering modal energies for case A where the FST is relatively low ($T_i = 1.84\%$). We propose a physical explanation for this behavior. While at $x/c = 5$ the intrinsic dynamics and instabilities of the vortex are weak in the reference case REF, they are overshadowed by turbulence effects in 'high' turbulence cases (B and C), leading to the emergence of other features such as deformations that absorb energy. In contrast, case A predominantly experiences vortex meandering with less interference from turbulence.

Employing Proper Orthogonal Decomposition (POD), the motion of the wing tip vortex is discerned independently of precise center detection and despite potential limited resolution within the vortex core. The POD analysis enabled us to enlighten some effects of FST on the vortex. FST accelerates the establishment of the vortex or at least its dynamics. Indeed, in the reference case REF, the signature of the wake remains prominent at $x/c = 5$; however, this is no longer the case for cases A, B, and C. Turbulence appears to induce the appearance of vortex deformation modes, while the vortex displacement mode remains predominant.

Finally, the investigation highlights the significance of streamwise position on vortex meandering amplitudes. While the current study mainly focuses on one station at $x/c = 5$ along the streamwise direction, future analyses will extend the domain to encompass a broader range, particularly at locations closer to the wing and farther downstream i.e. $x/c = 5$ and $x/c = 12$. One of the outlooks of this study includes spectral analysis using high-frequency data and investigating the relationship between wavelength, turbulence scale, and intensity.

REFERENCES

Bailey, S., Pentelow, S., Ghimire, H., Estejab, B., Green, M. & Tavoularis, S. 2018 Experimental investigation of the scaling of vortex wandering in turbulent surroundings. *J. Fluid Mech.* **843**, 722–747.

Ben Miloud, K., Dghim, M., Fellouah, H. & Ferchichi, M. 2020 Free-stream turbulence interaction with a wing-tip vortex. *J.Wind Engng. Ind. Aero.* **206**, 104211.

Bölle, T., Brion, V., Couliou, M. & Molton, P. 2023 Experiment on jet–vortex interaction for variable mutual spacing. *Phys. Fluids* **35** (1), 015117.

Devenport, W., Rife, M., Liapis, S. & Follin, G. 1996 The structure and development of a wing-tip vortex. *J. Fluid Mech.* **312**, 67–106.

Dghim, M., Ben Miloud, K., Ferchichi, M. & Fellouah, H. 2021 Meandering of a wing-tip vortex in a grid-generated turbulent flow. *Phys. Fluids* **33** (11).

Fabre, D., Sipp, D. & Jacquin, L. 2006 Kelvin waves and the singular modes of the lamb–oseen vortex. *J. Fluid Mech.* **551**, 235–274.

Gerz, T., Holzäpfel, F. & Darracq, D. 2002 Commercial aircraft wake vortices. *Prog. Aero. Sci.* **38** (3), 181–208.

Ghimire, H. & Bailey, S. 2017 An experimental investigation of wing-tip vortex decay in turbulence. *Phys. Fluids* **29** (3), 037108.

Hearst, R.J. & Lavoie, P. 2015 The effect of active grid initial conditions on high reynolds number turbulence. *Exp. Fluids* **56** (185).

Heyes, A. L., Jones, R. F. & Smith, D. A. R. 2004 Wandering of wing-tip vortices. *Proceedings of the 12th International Symposium on Applications of Laser Techniques to Fluid Mechanics.* Lisbon, Portugal, Paper 35-3.

Kildal, O., Li, L., Hearst, R.J., Petersen, Ø.W. & Øiseth, O. 2023 On the use of an active turbulence grid in wind tunnel testing of bridge decks. *J. Wind Engng. Ind. Aero.* **233**, 105331.

Larssen, J.V. & Devenport, W.J. 2011 On the generation of large-scale homogeneous turbulence. *Experiments in Fluids* **50**, 1207–1223.

Leweke, T. & Le Dizès, S.and Williamson, C. H.K. 2016 Dynamics and instabilities of vortex pairs. *Annu. Rev. Fluid Mech* **48**, 507–541.

Makita, H. 1991 Realization of a large-scale turbulence field in a small wind tunnel. *Fluid Dyn. Res.* **8**, 53–64.

Pentelow, S. 2014 Wing-tip vortex structure and wandering. Ph.D. thesis, Université d'Ottawa.

Sarpkaya, T. & Daly, J.J. 1987 Effect of ambient turbulence on trailing vortices. *J. Aircraft* **24** (6), 309–404.

Sirovich, L. 1987 Turbulence and the dynamics of coherent structures. i. coherent structures. *Quarterly of Applied Mathematics* **45**, 561–571.

Spalart, P. R. 1998 Airplane trailing vortices. *Annu. Rev. Fluid Mech.* **30** (1), 107–138.

Taira, K., Brunton, S. L., Dawson, S. T., Rowley, C. W., Colonius T.and McKeon B. J., T., Schmidt O., S., Gordeyev, V., Theofilis & S., Ukeiley L. 2017 Modal analysis of fluid flows: An overview. *AIAA Journal* **55**, 4013–4041.